A Spectroscopically-Validated Computational Investigation of Viable Reaction Intermediates in the Catalytic Cycle of the Reductive Dehalogenase PceA

Elizabeth D. Greenhalgh[†], Cindy Kunze[‡], Torsten Schubert[‡], Gabriele Diekert[‡], Thomas C. Brunold[†,*]

†-Department of Chemistry, University of Wisconsin-Madison, Madison, Wisconsin 53706, United States

‡-Department of Applied and Ecological Microbiology, Institute of Microbiology, Friedrich Schiller University, 07743 Jena, Germany

ABSTRACT: Organisms that produce reductive dehalogenases (RDases) utilize halogenated aromatic and aliphatic substances as terminal electron acceptors in a process termed organohalide respiration. These organisms can couple the reduction of halogenated substances with the production of ATP. Tetrachloroethylene reductive dehalogenase (PceA) catalyzes the reductive dehalogenation of per- and tri-chloroethylenes (PCE and TCE, respectively) to primarily *cis*-dichloroethylene (DCE). The enzymatic conversion of PCE to TCE (and subsequently DCE) could potentially proceed via a mechanism with the first step involving a single electron transfer, nucleophilic addition followed by chloride elimination or protonation, or direct attack at the halogen. Difficulties with producing adequate quantities of PceA have greatly hampered direct experimental studies of the reaction mechanism. To overcome these challenges, we have generated computational models of resting and TCE-bound PceA using quantum mechanics/molecular mechanics (QM/MM) calculations and validated these models on the basis of experimental data. Notably, the norpseudo-cob(II)alamin (Co(II)Cbl[*]) cofactor remains five-coordinate upon substrate-binding to the enzyme, retaining a loosely bound water on the lower face. Thus, the mechanism for the thermodynamically challenging Co(II)→Co(I)Cbl[*] reduction used by PceA differs fundamentally from that utilized by adenosyltransferases (ATRs), which generate four-coordinate Co(II)Cbl species to facilitate access to the Co(I) oxidation state. The same QM/MM computational methodology was then applied to viable reaction intermediates in the catalytic cycle of PceA. The intermediate predicted to possess the lowest energy is the one resulting from electron transfer from Co(I)Cbl[*] to the substrate to yield Co(II)Cbl[*], a chloride ion, and a vinylic radical.

Introduction

Organisms that contain reductive dehalogenases (RDases) utilize halogenated aromatic and aliphatic substrates as terminal electron acceptors in a process termed organohalide respiration. [1,2] These organisms are able to couple the reduction of halogenated substrates from human pollution or natural processes (such as those produced by algae, sponges, and fungi[3,4]) with a chemiosmotic production of ATP.[1,5] Since organisms that contain RDases occur in a variety of habitats including marine environments, oil reservoirs, and sewage plants where persistent halogenated compounds are found,[6,7] RDases naturally aid bioremediation by converting halogenated compounds that are toxic or carcinogenic to less toxic derivatives.[8]

Tetrachloroethylene (also known as perchloroethylene) reductive dehalogenase, PceA, is one such RDase found in *Sulfurospirillum multivorans*.[6] PceA is a norpseudo-cobalamin (Cbl[*]) and [4Fe-4S] cluster containing enzyme that primarily catalyzes the stepwise reduction of perchloroethylene (PCE), a carcinogenic industrial solvent, and trichloroethylene (TCE), a toxic dry-cleaning agent, to cis-dichloroethylene (DCE). As is the case for other organohalide respiring bacteria, *S. multivorans* is capable of performing the de novo biosynthesis of its unique corrinoid, Cbl[*], which lacks a methyl group at position 176 of the nucleotide loop and features an adenine in place of the 5,6-dimethylbenzimidazole intramolecular base that is present in cobalamins.[9,10]

The enzymatic conversion of PCE to TCE (and subsequently to DCE) could potentially proceed via a mechanism that begins with a single electron transfer (SET), nucleophilic addition, or direct attack at the halogen (Figure 1). In each case, the resting state Co(II)Cbl[*] is reduced to the catalytically relevant Co(I)Cbl[*] species by electron transfer through the two [4Fe-4S] clusters.[11] Supported by X-ray crystal structures of PceA incubated with halogenated phenol substrates[12] and radical trapping of propene reaction intermediates,[13] the SET reaction proceeds via electron transfer from Co(I)Cbl[*] to the substrate, yielding Co(II)Cbl[*], a chloride ion, and a vinylic radical (Figure 1, eq 1). The vinylic radical is further reduced either through a transiently formed Co(I)Cbl[*] species or directly from a $[4Fe\text{-}4S]^{1+}$ cluster, and then protonated to form TCE. The proton donor in PceA has not been definitively identified but has been presumed to be the Y246 residue conserved across reductive dehalogenases.[11]

While carbon isotope fractionation factors appear to support the SET mechanism, these factors, as well as carbon and chlorine isotope effects, are also consistent with a mechanism

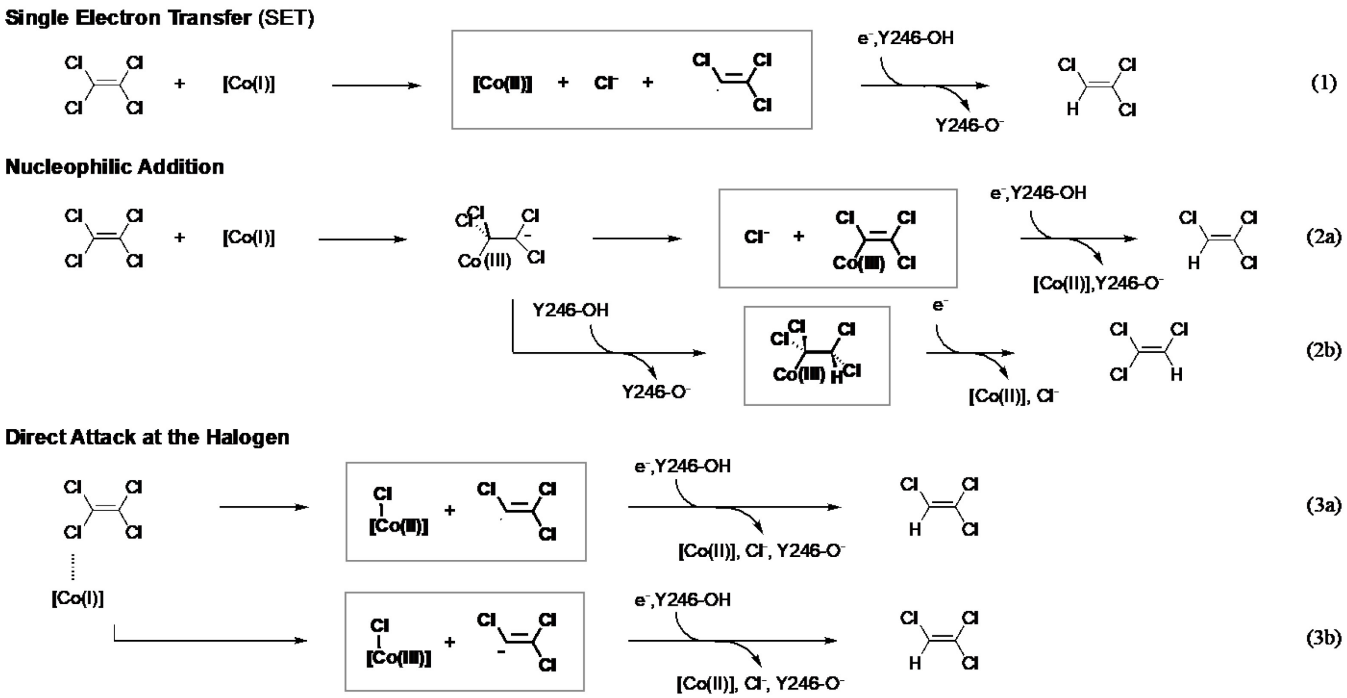

involving either nucleophilic addition followed by elimination or nucleophilic addition with subsequent protonation as the first step in trichloroethylene dechlorination.[14–16] In the nucleophilic addition mechanisms, catalysis is instigated by attack of the reduced Co(I) center on one of the two equivalent carbon atoms of the substrate, forming a carbanion intermediate. This intermediate can subsequently undergo chloride elimination (Figure 1, eq 2a) or protonation (Figure 1, eq 2b). Further one-electron reduction in conjunction with protonation or chloride elimination promotes formation of Co(II)Cbl* and TCE.

The third mechanistic proposal invokes direct attack of the Co(I)Cbl* species on a substrate halogen to form a Co–Cl adduct that undergoes either homolytic Cl–C bond cleavage (Figure 1, eq 3a), yielding a vinylic radical and a Cl–Co(II)Cbl* species, or heterolytic Cl–C bond cleavage (Figure 1, eq 3b), forming a carbanion and Cl–Co(III)Cbl*. Further one-electron reduction and protonation results in both pathways converging to Cl–Co(II)Cbl* and TCE. A previous computational study of PceA comparing homolytic and heterolytic cleavage of the Co–Cl adduct revealed that heterolytic Cl–C bond cleavage to yield Cl–Co(III)Cbl* is energetically more favorable.[17] A direct attack of the Co(I) center on a substrate halogen has been proposed for *Nitratireductor pacificus* pht-3B RdhA, a similar reductive dehalogenase that primarily reduces halogenated phenols.[18] EPR studies of *Np*RdhA revealed ^{79}Br and ^{81}Br super-hyperfine splittings of the Co(II)Cbl signals, providing evidence of a direct halide-cobalt interaction in this enzyme.[18] Additionally, a similar mechanism was established for base-promoted cleavage of aryl–halogen bonds by Co(II)porphyrins,[19] a family of related tetrapyrroles.

Difficulties with heterologous gene expression, low growth yields, and the oxygen sensitivity of PceA have greatly hampered direct experimental studies of the PceA reaction mechanism.[9,11,20] To overcome these challenges, we have collected magnetic circular dichroism (MCD) data of PceA in the absence and presence of substrate, generated computational models of these states using the quantum mechanics/molecular mechanics (QM/MM) method, and validated our models on the basis of the experimental data. Computational models of viable reaction intermediates were then prepared using the same computational methodology. A comparison of the structures and relative energies of these species models provides a means to assess the feasibility of previously proposed reaction mechanisms employed by PceA to convert PCE to TCE.

Experimental Methods

Protein Production. S. multivorans PceA containing Co(II)Cbl* was isolated and purified as previously described.[11] Protein was stored at -80 °C in 30-40 mM Tris-HCl, pH 7.5 buffer.

Sample Preparation. All chemicals were purchased from Sigma and used as received without further purification. Water was purified by reversed osmosis followed by ion exchange and filtration steps on a Millipore Milli-Q water purification system.

Titanium(III) citrate was prepared according to a published method[21] by the reaction of 15% $TiCl_3$ (in 10% HCl solution) with sodium citrate tribasic dehydrate in a 1:2 molar ratio, followed by neutralization with saturated sodium carbonate in an anaerobic atmosphere to yield a dark red-brown liquid. Absorption spectroscopy was used to verify the oxidation state of the product on the basis of a published reference spectrum.[22]

Diaquacobinamide [$(H_2O)_2Cbi^{2+}$] was prepared by adding the reductant $NaBH_4$ to an aqueous solution of $(CN)_2Cbi$, loading the reaction mixture on a C18 SepPack column, washing with H_2O, and eluting the product with methanol, as described in a previous report.[23] $(H_2O)_2Cbi^{2+}$ was then reduced to $Co(II)Cbi^+$ in an anaerobic environment via dropwise addition of saturated potassium formate in buffer. Absorption spectroscopy was used to verify the oxidation state of the product and determine its concentration using Beer's Law via the reported molar extinction coefficient for $Co(II)Cbi^+$ of 11 $mM^{-1}cm^{-1}$ at 470 nm.[24]

Electronic Absorption and Magnetic Circular Dichroism Spectroscopies. Room temperature electronic absorption (Abs) spectra were obtained using a Varian Cary 5e spectrophotometer. For oxygen sensitive samples, the sample compartment was purged with N_2 gas for 40 min prior to use. Low temperature Abs, circular dichroism (CD), and magnetic CD (MCD) spectra were collected with a JASCO J-715 spectropolarimeter in conjunction with an Oxford Instruments SM-4000 8 T super conducting magnetocryostat. For low-temperature studies, samples were prepared to a final concentration between 115-165 µM with 55-60% (v/v) glycerol to ensure glass formation upon freezing in liquid nitrogen. CD background and glass-strain contributions to the MCD spectra were removed by taking the difference between spectra collected with the 7 T magnetic field oriented parallel and anti-parallel to the axis of light propagation.

Generation of Computational Models and Time Dependent-Density Functional Theory Computations. All quantum mechanics/molecular mechanics (QM/MM) optimizations were performed using the ONIOM method as implemented in Gaussian09.[25] Published high-resolution (1.65 Å) X-ray crystallographic data of *S. multivorans* PceA bound with *cis*-dibromoethylene (DBE) (PDB entry 4ur1) were used as initial coordinates.[11] PDB2PQR[26] was employed to add hydrogen atoms to all residues at a pH of 7.0. Hydrogen atoms were added manually to $Co(II)Cbl^*$ using the PyMOL molecular graphics system.[27] While the crystal structure indicates PceA is a homodimer, the two active sites are separated by 42 Å (Co–Co distance) with no cofactors or substrate channel between them.[11] This indicates the two dimers function as independent subunits, warranting *in silico* study of only one monomer. Additionally, residues 417-431 were not resolved in the X-ray crystal structure, causing residues 431-461 to be disconnected from the rest of the enzyme. As these residues are far from the active site, they were removed from our models to avoid issues with the optimization. The QM region consisted of Cbl^* with each sidechain truncated after the first carbon atom[28] (with the exception of the sidechain closest to the substrate, see Figure S1), axial water, and substrate, where applicable, along with amino acid residues Y246, N272, and R305. These residues were included in the QM region due their highly conserved nature among reductive dehalogenases[11] as well as their location in the enzyme active site. The QM region was treated with the BP86 functional[29,30] and TZVP basis set.[31] The remainder of the enzyme was modeled using MM with the AMBER forcefield.[32] Bonds that cross the boundary between the QM and MM regions were treated with a capping hydrogen atom with C–C bond lengths scaled by 0.709. AMBER parameters for the cobalamin were taken from the literature.[33] The original model (generated using coordinates from PDB entry 4ur1) was first optimized with a pure MM method prior to ONIOM based geometry optimizations. The default ONIOM convergence criteria were used for all models. The models were optimized using a charge and multiplicity consistent with low-spin Co(II) species for the resting and substrate bound states (total S=1/2), low-spin Co(III) species for the intermediates involving nucleophilic addition and Co–Cl adduct formation via heterolytic Cl–C bond cleavage (total S=0), or low-spin Co(II) species for the intermediates formed upon SET and Co–Cl adduct formation and homolytic Cl–C bond cleavage (total S=1). The root mean square deviation (rmsd) of atomic positions between the optimized models and published crystal structures were determined using the align method in PyMOL.[27] Figures for all models were created using PyMOL.[27]

After convergence of the QM/MM geometry optimizations, the coordinates of the QM region (truncated Cbl^*, axial water, and substrate, where applicable, along with residues Y246, N272, and R305) were extracted for time-dependent density functional theory (TD-DFT) calculations using the ORCA4.0 computational package.[34] Protein residues were truncated at their beta carbons and capped with hydrogens. TD-DFT calculations were performed with the camB3LYP[35] and wB97[36] functionals. The def2-SVP[37] and def2/J[38] basis sets were employed for all atoms except for Co and all coordinating atoms, for which the TZVP[39] basis set was employed. The RIJCOSX approximation as implemented in ORCA4.0 was used to speed up the calculation of the Hartree-Fock exchange term. With the exception of the capping atoms explicitly replaced with H-atoms, all MM atoms were included in the computations as point charges with values defined by the force field used in the QM/MM optimization. The TD-DFT calculation for $Co(II)Cbi^+$ was performed with CPCM water solvation. Isosurface plots of electron density difference maps (EDDMs) were prepared in PyMOL using isodensity values of ±0.05 au.[27] Corrin ring distortion parameters were calculated as described elsewhere.[40,41]

Results

Spectroscopy. The electronic absorption (Abs) spectrum of PceA exhibits several overlapping bands in the visible and near-UV regions (Figure 2). These features arise from electronic transitions localized on the $Co(II)Cbl^*$ species and two $[4Fe\text{-}4S]^{2+}$ clusters. More information concerning the Co-ligand environment can be obtained using magnetic circular dichroism (MCD) spectroscopy due to the signed nature of the MCD signal and the much higher relative intensity at low temperature of features arising from the paramagnetic $Co(II)Cbl^*$ species compared to those from the diamagnetic $[4Fe\text{-}4S]^{2+}$ clusters. Furthermore, through the mechanism of spin-orbit coupling, the Co(II) ligand field (or d→d) transitions that are parity-forbidden in Abs spectroscopy gain significant MCD intensity. Because the singly occupied Co $3d_{z^2}$-based molecular orbital is oriented perpendicular to the corrin ring of $Co(II)Cbl^*$, the ligand field transitions are particularly sensitive to changes in the axial ligand environment. These transitions have been previously shown to dominate the low-energy region of the MCD spectrum.[42]

Consistent with published X-ray crystal structures,[11] the MCD spectrum of as-isolated PceA indicates that the cobalt center of $Co(II)Cbl^*$ is five-coordinate with the intramolecular base replaced by a water molecule in one of the axial positions (Figure 3). The lowest energy feature, which arises from a Co(II) ligand field transition that is especially sensitive to changes in the Co-axial ligand interaction,[42] is red-shifted by ~320 cm^{-1} from its counterpart in the MCD spectrum of

Co(II)cobinamide$^+$ (Co(II)Cbi$^+$, a mimic of base-off Cbl at neutral pH that lacks the lower nucleotide loop and intramolecular base), indicating a weaker Co–O(H_2) bond in the protein-bound Co(II)Cbl*. Due to the high similarity between the shape of the spectrum of as-isolated PceA and Co(II)Cbi$^+$, it is clear that PceA binds Co(II)Cbl* without major conformational changes of the corrin ring.

Addition of TCE to PceA causes only minor changes to the MCD spectrum, ruling out any major conformational changes of the Co(II)Cbl* species. While the lowest energy feature is slightly broadened in the presence of TCE, possibly reflecting some variability in the axial Co–OH_2 bond distance, our data provide compelling evidence that the PceA-bound Co(II)Cbl* species remains five-coordinate even in the presence of substrate. Further differences between the MCD spectra of PceA in the absence and presence of TCE include a modest red-shift of the metal to ligand charge transfer (MLCT) transition at 20,030 cm^{-1} upon addition of substrate. As this MLCT transition arises from excitations between the filled Co 3d-based and empty corrin π*-based molecular orbitals (MOs),[42] the observed red-shift likely signifies a small change in the corrin ring conformation upon TCE binding to the enzyme active site.

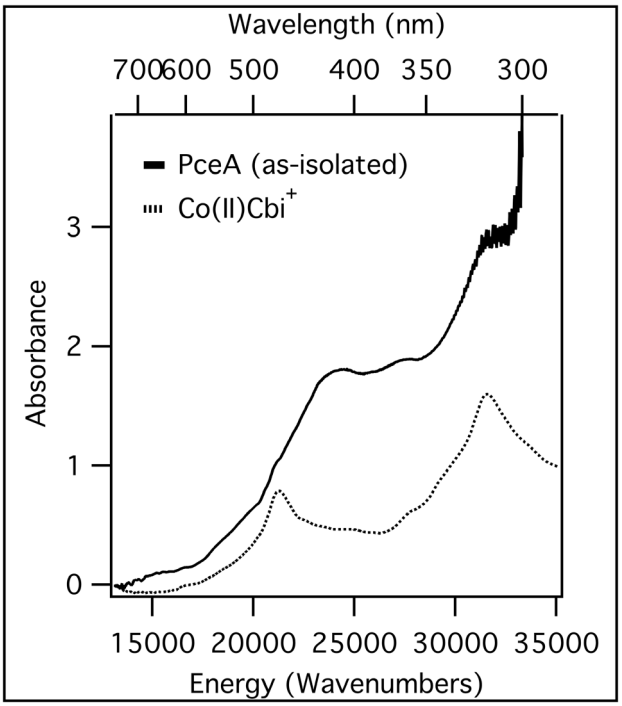

Figure 2. Abs spectra at 4.5 K of as-isolated PceA (solid line) and Co(II)Cbi$^+$ (dotted line).

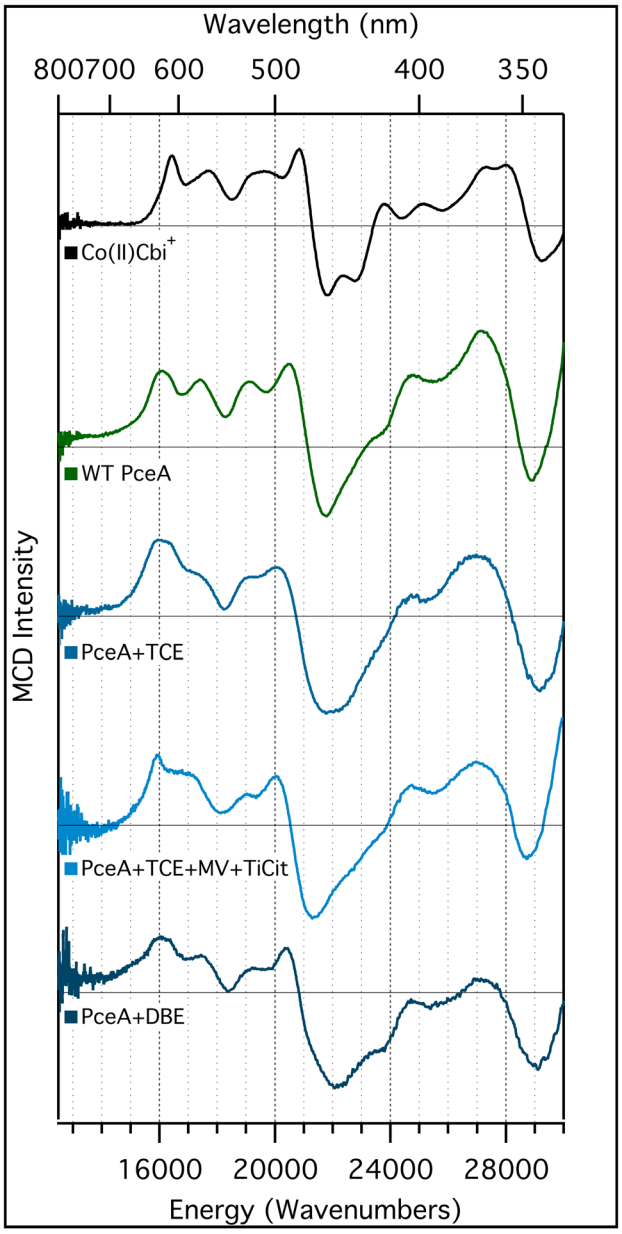

Figure 3. MCD spectra at 4.5 K and 7 T of (from top to bottom) Co(II)Cbi$^+$; as-isolated PceA, PceA incubated with TCE; PceA incubated with TCE, titanium citrate, and methyl viologen; and PceA incubated with DBE.

the Co(II)Cbl* cofactor. These predictions are consistent with the crystal structure of DBE-bound PceA (PDB entry 4ur1), which revealed that DBE does not displace the axial water ligand of Co(II)Cbl* and binds with both bromine atoms pointing away from the Co center.

QM/MM Geometry Optimizations. A whole-protein model of PceA in the absence of substrate was generated by performing a QM/MM optimization starting from a published high-resolution X-ray crystal structure of PceA bound with DBE (see Methods section). The rmsd of atomic positions between the optimized model and the crystal structure of 0.949 Å (comparing 2553 non-hydrogen atoms) falls below the resolution of the crystal structure, 1.65 Å,[11] indicating that the QM/MM optimized model is in good agreement with the atomic positions captured in the crystallographic coordinates. The most notable difference in the active site region between the experimental (PDB entry 4uqu) and computed structures of substrate-free PceA (Figure 4, A and B) involves a minor rotation of Y246, the presumed proton donor during catalysis, such that the -OH group extends slightly further over the face of the cobalamin in the computational model. Interestingly, in the crystal structure of resting PceA (PDB entry 4uqu[11]), water molecules are present both above and below the Co(II) ion (Figure 4), though the Co(II)Cbl* species is expected to possess a single axial ligand. Indeed, our optimized model shows that only the water molecule in the lower axial position coordinates to the Co(II) ion, while the water above the upper face is rotated to participate in a hydrogen bond network.

Optimization of a PceA model with TCE added to the active site *in silico* yielded a geometry in good agreement with the crystal structure of TCE-bound PceA (PDB entry 4ur0[11]), with a rmsd of atomic positions of 0.749 Å (comparing 2559 non-hydrogen atoms) that is again well below the resolution of the crystal structure, 1.80 Å.[11] Although the orientation of the substrate in the QM/MM optimized model differs somewhat from that observed experimentally, the distance between the Co(II) ion and proximal carbon atom of TCE is well reproduced (Figure 4, C and D).

Addition of an electron to the TCE-bound PceA model containing Co(II)Cbl* yielded a Co(I)Cbl* species. As expected, during the QM/MM optimization of this model, the water molecule in the lower axial position of the Co(I) center moved away to yield a four-coordinate Co(I)Cbl* species (Table 1). This model is particularly noteworthy given the lack of any (free or enzyme-bound) Co(I)Cbl crystal structure.

Validation of the Computational Models on the Basis Spectroscopic Results. While Abs spectroscopy is poorly suited for characterizing the PceA-bound Co(II)Cbl* species, the MCD data obtained in this study provide an excellent framework for validating computational models. Importantly, the QM/MM optimized models of substrate-free and TCE-bound PceA both feature five-coordinate Co(II)Cbl* with a water molecule occupying the lower axial position, as stipulated by the close resemblance of the MCD spectra obtained for these species and free Co(II)Cbi$^+$ (Figure 3). Moreover, time-dependent density functional theory (TD-DFT) calculations performed on the QM region of the computational models predict a moderate red-shift of the lowest-energy transitions from Co(II)Cbi$^+$ to PceA-bound Co(II)Cbl* (Figure 5), consistent with our MCD spectra (Figure 3). To ascertain that the TD-DFT computations correctly describe these transitions as involving primarily Co(II) d→d excitations, electron density difference maps (EDDMs) were calculated that provide a visual representation of the change in total electron density upon electronic excitation (Figure 5, bottom). Inspection of these EDDMs reveals that the two lowest-energy transitions correspond to the Co(II) $d_{yz}\rightarrow d_{z2}$ and $d_{xz}\rightarrow d_{z2}$ excitations. The red-shift of these transitions from Co(II)Cbi$^+$ to PceA-bound Co(II)Cbl* predicted computationally and observed experimentally may arise from the presence of a water molecule that hydrogen-bonds to the Co(II) ion in the latter, which leads to a stabilization of excited states arising from electronic excitations terminating in the Co(II) d_{z2} orbital. The overall good agreement between the structures and spectroscopic properties predicted for our computational models of PceA in the presence and absence of substrate and available experimental data warranted the use of the same computational methodology for generating models of viable reaction intermediates.

Computational Models of Potential Reaction Intermediates. To establish the most probable mechanism for the reduction of PCE employed by PceA, a model was generated via QM/MM geometry optimization of the key intermediate for each mechanism as highlighted in Figure 1. While no crystal structures are available for a direct evaluation of these models, certain geometric parameters can be compared to the experimentally validated QM/MM optimized structure of TCE-bound PceA and other published data to ensure the optimized intermediates have reasonable geometries (Table 1).

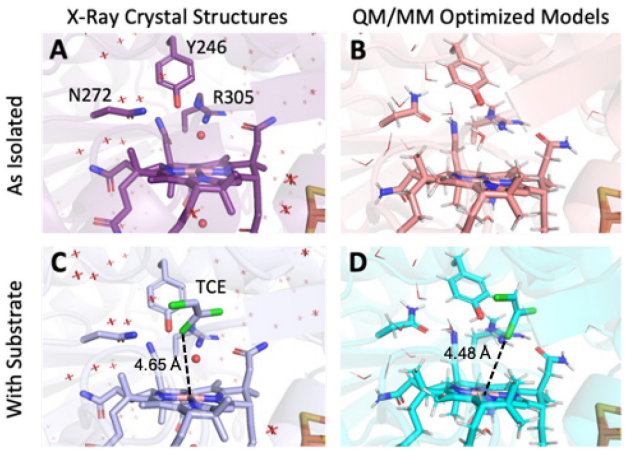

The distance between the Co ion and lower axial water varies from 3.7 Å in the computational models where the water would not be expected to coordinate (such as the nucleophilic addition pathways) to 2.5 Å in the SET intermediate model, in which the water molecule remains coordinated. These values align well with the axial Co–O distances of ~2.5 – 3.6 Å in a crystal structure of resting PceA (PDB entry 4uqu[11]) to 2.4 Å in the QM/MM optimized model of TCE-bound PceA. The Co–Cl distances for the mechanisms involving direct attack of the Co(I) center on the halogen suggest that a bond has formed, which is also reflected in the increased C– Cl(leaving) distances. Specifically, the Co(II)–Cl bond

Table 1. Key Bond Distances and Angles for Optimized Computational Models

	PceA	PceA + TCE	PceA + TCE	Single Electron Transfer	Nucleophilic Addition Protonate	Nucleophilic Addition Eliminate	Cl-Adduct Heterolytic Cleavage	Cl-Adduct Homolytic Cleavage
Co Oxidation State	Co^{II}	Co^{II}	Co^{I}	Co^{II}	Co^{III}	Co^{III}	Co^{III}	Co^{II}
Bond Distances (Å)								
Co-Lower Axial Water	2.40	2.40	3.68	2.49	3.68	3.68	3.69	3.48
Co-Substrate Cl	-	4.48	3.75	7.17	-	6.59	2.84	2.59
Co-Substrate C	-	6.20	5.49	6.22	2.03	1.95	4.70	5.55
C-Leaving Cl	-	1.75	1.75	4.77	-	5.56	1.87	3.30
Ring Distortion Parameters								
ring fold angle (°)	14.96	10.67	13.88	16.6	9.67	14.63	12.83	15.21
helicity, *h* (°)	4.51	2.84	2.86	2.52	5.83	1.79	2.52	2.26
interplanar angle (°)	5.94	5.85	6.08	5.02	25.67	23.98	12.68	8.18

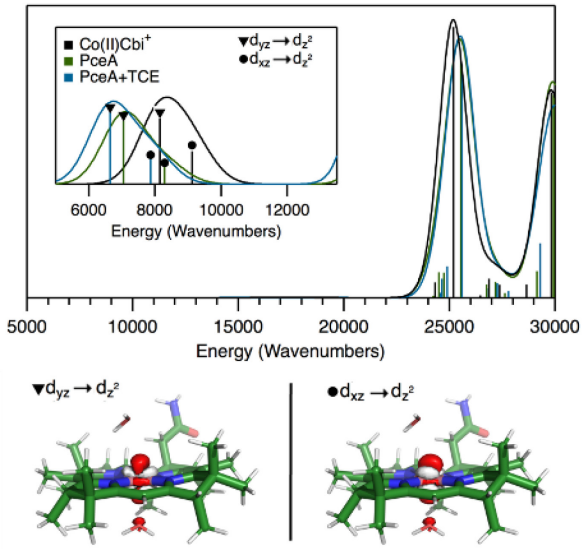

Figure 5. Top: TD-DFT computed Abs spectra for the QM region of the QM/MM optimized models of Co(II)Cbi^{+} (black), resting PceA (green), and TCE-bound PceA (blue). The inset shows the low-energy region with the Abs intensities scaled by a factor of 500. Bottom: Electron density difference maps (EDDMs) for the two lowest-energy Co(II)Cbl^{*} d→d transitions of resting PceA (also representative of the other two species). Gray and red represent a loss and gain of electron density, respectively.

length of 2.59 Å in the model for the intermediate formed in the homolytic C–Cl bond cleavage pathway is consistent with published Co–Cl bond distances,[11,18] including the Co(II)–Cl bond distance of 2.5 Å reported for *Np*RdhA (PDB entry 4ras[18]), as well as the Co(II)–I bond distance of 2.9 Å observed for PceA (PDB entry 4ur2[11]). However, the distance of 3.69 Å between the Co(III) ion and the lower axial water in the model of the intermediate formed upon heterolytic C–Cl bond cleavage is considerably longer than would be expected for a six-coordinate Co(III) complex, and so is the Co–Cl bond distance of 2.84 Å, while the relatively short C–Cl distance of 1.87 Å indicates that this bond is not fully broken. Notably, a QM/MM geometry optimization of an additional model of PceA-bound Cl-Co(III)Cbl^{*} in which both the Co–Cl and Co–OH_2 bonds were shortened converged to a Co(I) species, providing further evidence that the pathway involving direct attack of the Co(I) center on the halogen followed by heterolytic C–Cl bond cleavage is energetically unfavorable. Although it is difficult to assess the feasibility of the SET intermediate structure directly, the distance between the Co(II) ion and the proximal C atom of the substrate and Co(II)Cbl^{*} conformation in this intermediate are similar to their counterparts in the optimized structure of TCE-bound PceA, as expected. Lastly, the intermediates associated with the nucleophilic addition mechanisms both have a Co(III)–C bond distance of 2.0 Å, identical to that in the methylcobalamin dependent methionine synthase (PDB entry 1bmt[45]).

The overall distortion of the corrin ring for each intermediate was analyzed using a variety of established parameters (Figure 6), including corrin fold angle (the angle between the planes formed by N21, C4, C5, C6, N22, C9, and C10 and N24, C16, C15, C14, N23, C11, and C10),[46] helicity (the dihedral angle of the four central corrin nitrogen atoms), and interplanar angle (the angle between the planes formed by N21, N22, and Co and N23, N24, and Co).[41] The corrin fold angle is most informative of the conformational changes along the Co···C10 axis in base-on Co(III)Cbls.[46] While less informative for Co(II)Cbl species, the corrin fold angles for the models of the intermediates containing Co(II)Cbl^{*} are within published

ranges (Table 1).[47] The *trans* nature of the juncture between rings A and D of the corrin macrocycle introduces a helical arrangement for the four central nitrogen atoms.[48] Metal free corrin (hydrogenobyric acid) displays the largest helicity, 12.9°, while Co(II)Cbl and all Co(III)Cbls exhibit reduced helicity values because the corrin flattens to better accommodate the square pyramidal and octahedral coordination preferences of Co(II) and Co(III) ions, respectively.[41] The helicity values determined for our computational models of the PceA reaction intermediates generally deviate only marginally from 0°, reflecting an essentially planar arrangement of the four coordinating nitrogen atoms of the corrin ring. The two outliers are the models of the addition pathway intermediates, where direct bond formation between the Co(III) ion and dehalogenated substrate induces more strain in the corrin ring. This perturbation can be further understood through analysis of the corrin interplanar angle, which characterizes the distortion of the coordination environment of the Co center. Coordinative strain is indicated by deviation of the interplanar angle from 0°, the limit for square pyramidal and octahedral geometries.[41] The majority of the models have small interplanar angles, indicating that the Co ion resides in nearly the same plane as the equatorially ligating nitrogen atoms. Yet, the models for the addition pathway intermediates are again the outliers and instead have interplanar angles near 25°. This result further highlights the steric clashes that exist between the bound substrate and corrin ring in these organometallic intermediates.

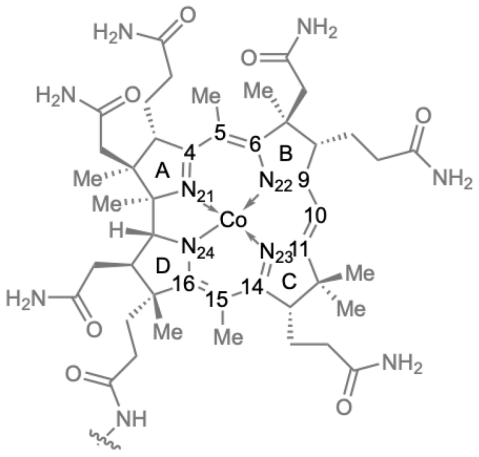

Figure 6. Truncated structure of norpseudo-Cbl and atom numbering used to define the corrin fold angle (the angle between the planes formed by N21, C4, C5, C6, N22, C9, and C10 and N24, C16, C15, C14, N23, C11, and C10),[46] helicity (the dihedral angle of the four central corrin nitrogen atoms), and interplanar angle (the angle between the planes formed by N21, N22, and Co and N23, N24, and Co).

Since the optimized geometries for the reaction intermediate models are consistent with available crystallographic data and are reasonable as judged on the basis of the structural considerations presented above, a comparison of the ONIOM extrapolated relative energies is warranted (see Figure 7). The intermediate predicted to possess the lowest energy is the one resulting from electron transfer from Co(I)Cbl* to the substrate (SET mechanism), yielding Co(II)Cbl*, a chloride ion, and a vinylic radical. Alternatively, the models of the intermediates following Co–Cl adduct formation and heterolytic Cl–C bond cleavage or homolytic Cl–C bond cleavage have the highest relative energies of 54.2 kcal/mol and 65.8 kcal/mol (as described above, the latter may not correspond to a true intermediate). These high, but not unreasonable, energies suggest that the mechanism utilized by PceA likely does not proceed through an attack of the Co(I) ion on a substrate halogen. In fact, the relative energy of the TCE-bound PceA model containing Co(I)Cbl* of 53.8 kcal/mol is lower than the relative energies of the intermediates formed upon direct attack of the Co(I) center on a substrate halogen. Yet, the intermediate following heterolytic Cl–C bond cleavage can be stabilized by protonation of the carbanion by Y246, as proposed by Liao et al.[17] Indeed, when we transferred the phenolic proton from Y246 to the carbanion and reoptimized the geometry, Y246 accepted a proton from R305 and the relative energy of this model decreased to 36.0 kcal/mol (still disfavoring this pathway). Finally, the model of the intermediate generated via nucleophilic attack of the Co(I) ion on the proximal substrate carbon atom followed by elimination has a relative energy of 35.1 kcal/mol, while the model for the nucleophilic addition/protonation intermediate (with R305 again serving as the ultimate proton donor) is 16.7 kcal/mol higher in energy than the SET intermediate. Note that because homolytic cleavage of the Co–C bond in the nucleophilic addition/elimination intermediate formally leads to the SET intermediate, the Co–C bond dissociation energy in the former is seemingly –35.1 kcal/mol. This negative value reflects the large steric strain that is present in the intermediates resulting from direct Co–C bond formation and the favorable interactions between the substrate (radical) and active site residues that exist when TCE is positioned farther away from the Co center (as in the crystal structure of TCE-bound PceA, Figure 4C).

Discussion

Resting PceA and Effect of Substrate Binding. The X-ray crystal structures of PceA in the absence and presence of substrate show that Co(II)Cbl* is bound base-off with a water molecule occupying an axial position.[11] These structures also indicate that the active site cavity is lined primarily by tyrosine and tryptophan residues, with Y246 situated within hydrogen bonding distance of TCE in the substrate-bound PceA crystal structure. The QM/MM optimized models for as-isolated and TCE-bound PceA faithfully reproduce the key structural features of the active site as observed in the crystal structures.[11] Consistent with these structures and our MCD data, the computational models feature base-off Co(II)Cbl* with a slightly elongated Co–O(H_2) bond. Further, the QM/MM optimized models indicate that Y246 is positioned to serve as a proton donor during enzyme turnover, with the guanidinium group of R305 having the correct orientation to stabilize the anionic, deprotonated form of Y246.

Importantly, no direct interaction between the substrate Cl atoms and Co(II)Cbl* is observed in the crystal structure of TCE-bound PceA[11] Consistent with this structure and our MCD data, the corresponding computational model shows that the Co(II)Cbl* cofactor remains five-coordinate upon substrate-binding to the enzyme, retaining a loosely bound water on the lower face. Thus, the mechanism for the thermodynamically challenging Co(II)→Co(I)Cbl* reduction used by PceA differs fundamentally from that utilized by adenosyltransferases (ATRs), which catalyze the Co–C bond formation step dur-

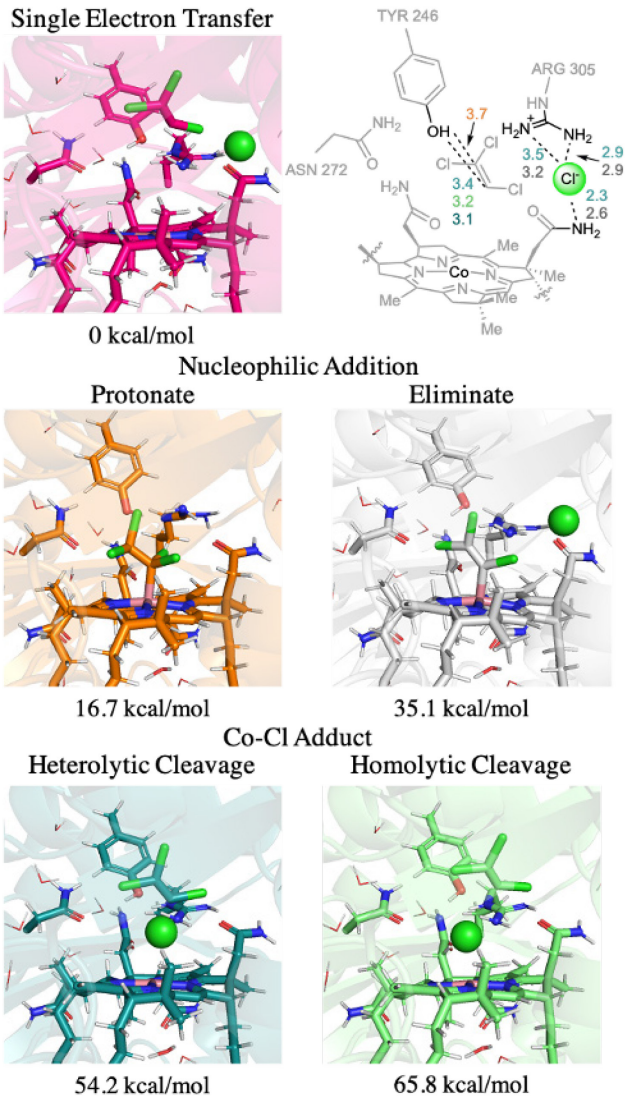

Figure 7. Computed relative energies and relevant portions of optimized active site geometries for key intermediates of the different reaction mechanisms evaluated in this work. Top right: key distances (in Å) not included in Table 1 (pink, SET; orange, nucleophilic addition protonation; gray nucleophilic addition elimination; teal, Co–Cl adduct formation with heterolytic Cl–C bond cleavage; green, Co–Cl adduct formation with homolytic Cl–C bond cleavage). Note that the relative energy of the intermediate formed via Co–Cl adduct formation and heterolytic Cl–C bond cleavage is reduced to 36.0 kcal/mol when the carbanion is protonated (see text).

ing adenosylcobalamin biosynthesis.[49–51] Upon addition of co-substrate ATP, ATRs force Co(II)Cbl into a four-coordinate conformation, effectively lowering the thermodynamic barrier for Co(II)-ion reduction. In contrast to ATRs, the corrinoid/FeS protein utilizes a low potential [4Fe-4S] cluster to facilitate the reduction of the catalytically inactive Co(II)corrinoid species that is formed via oxidation of the Co(I) intermediate, which occurs in about 1 out of every 100 turnovers.[52] Similar to the corrinoid/FeS protein, PceA contains two low potential [4Fe-4S] clusters (approximately -440 mV versus standard hydrogen electrode) that serve as an internal reducing system.[9,53] While the physiological reductant remains unknown, the reduction potential of the Co(II/I)Cbl* couple is raised from -490 mV to -380 mV (versus standard hydrogen electrode) upon binding to PceA,[10] probably due to a Co–O(H_2) bond elongation as revealed by our MCD data, such that the [4Fe-4S]$^{1+}$ clusters are sufficiently potent to reduce PceA bound Co(II)Cbl*.

Computational Evaluation of Viable PceA Reaction Intermediates. Because direct experimental studies of the reaction mechanism employed by PceA for the reduction of PCE and TCE to DCE have been hampered by difficulties in producing adequate quantities of the enzyme, multiple reaction mechanisms have been proposed in the literature. In this study, we have generated whole-enzyme QM/MM models that were validated on the basis of experimental data to assess the feasibility of previously proposed reaction mechanisms.

Based on the relative energies of the computational models, the SET mechanism proceeds via the formation of the lowest-energy intermediate. This pathway has the added benefit of minimizing reorganization energies during turnover, as the vinylic radical in the computational model is found in nearly the same location as TCE in the model of substrate-bound PceA as well as both substrate and product in previously published X-ray crystal structures.[11] Support for similar positions of substrate and product in the enzyme active site is also provided by our MCD data, which indicate highly similar coordination environments for PceA-bound Co(II)Cbl* in the presence of TCE and DBE, a product analogue.

Our computational prediction that the SET pathway is the preferred mechanism for PceA is also consistent with other data in the literature. While a nucleophilic addition pathway was favored on the bases of carbon isotope fractionation factors along with carbon and chlorine isotope effects, it was noted in the original publication that the isotope fractionation factors could also support a SET mechanism.[16] Furthermore, the dual element isotope regression slopes did not evaluate a SET mechanism as a mechanistic option.[14] Support for the formation of a Co–Cl adduct arose primarily from EPR data collected for samples containing *Np*RdhA and various halogenated substrates.[18] These data revealed a direct interaction between the halogen and the Co. Since the data were collected with as-isolated enzyme, not the reduced form of the cofactor, it is unclear whether the Co–halogen interaction persists upon Co(II)Cbl reduction. Regardless, given the large (>4 Å) distance between the Co(II) ion and nearest Cl atom in the X-ray crystal structure[11] and computational model of TCE-bound PceA and on the basis of our MCD data, formation of a Co–halogen bond is unlikely to occur in PceA catalytic cycle. Although a previous computational study of PceA led to the proposal that the catalytic cycle involves Co–Cl adduct formation followed by heterolytic Cl–C bond cleavage, other potential mechanisms including SET were not evaluated in that study.[17,54]

Based on the computational models of the reaction intermediates in conjunction with an analysis of available X-ray crystal structures,[11] PceA variants Y382A or Y102A, T242A, and F38Y would be particularly good targets to allow for a further discrimination between viable reaction mechanisms once a suitable enzyme expression system has been developed to incorporate amino acid substitutions (Figure 8). Residues Y382 and Y102 serve to orient the nascent vinylic radical in the model of the SET intermediate. Substitution of either tyrosine with alanine should therefore drastically reduce the PceA

turnover rate if the SET pathway were indeed the preferred mechanism, and to a much lesser extent if any of the other mechanisms were operative. Alternatively, T242 serves to cap the pocket housing the Cl^- ion in the models for both the SET and the nucleophilic addition followed by Cl^- elimination intermediates. Thus, the mechanisms involving early loss of the Cl^- ion (i.e., SET and nucleophilic addition/elimination) should be particularly sensitive to the T242A substitution. Finally, the relatively bulky F38 lines the active site, limiting attack of the Co(I) ion on the closest carbon atom of substrate PCE in the early stages of the two nucleophilic addition pathways. The F38W substitution would increase the steric clash between residue 38 and TCE, effectively preventing the substrate from approaching the Co(I) ion while maintaining the substrate docking distance observed both in the TCE-bound PceA crystal structure and in the SET intermediate model. This substitution should therefore preferentially disfavor the nucleophilic addition pathways.

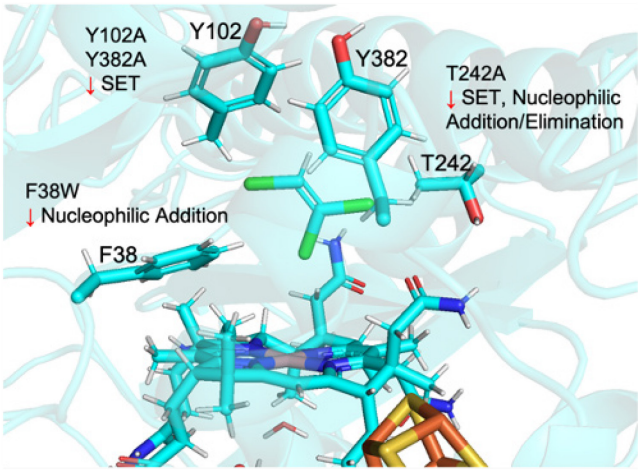

Figure 8. Proposed PceA amino acid substitutions and the reaction pathway(s) that would show the largest rate reduction by each substitution.

Conclusions

Because spectroscopic and biochemical studies of PceA have been hampered by difficulties in producing adequate quantities of this enzyme, we have generated computational models validated on the basis of X-ray crystallographic and spectroscopic data to assess the feasibility of previously proposed reaction mechanisms. While earlier studies have led to different conclusions as to the mechanism of enzymatic reductive dehalogenation, we have been able to rule out mechanisms involving a Co–Cl adduct in favor of a SET initiated reaction. Comparison of the various intermediate models permitted identification of amino acid residues serving important structural roles that could be targeted by site-direct mutagenesis to allow for a further discrimination between viable reaction mechanisms. In addition to assisting in the design of PceA variants for future spectroscopic and kinetics studies, this work also provides a solid foundation for similar computational studies on transition states and the final step of the reaction mechanism.

ASSOCIATED CONTENT

Supporting Information

The Supporting Information is available free of charge on the ACS Publications website.

Truncation of Cbl used for the QM region of the QM/MM optimizations and TD-DFT calculations, temperature dependence of MCD data, and computed Co spin densities for spin unrestricted QM/MM models (PDF), as well as coordinates for the QM region of all models (XLS).

Accession Code

PceA from *Sulfurospirillum multivorans*: UniProt O68252.

AUTHOR INFORMATION

Corresponding Author

* E-mail: brunold@chem.wisc.edu. Phone: (608) 265-9056.

Author Contributions

E.G. and T.B. designed the experiments and wrote the manuscript. E.G. performed all experiments. C.K. produced PceA under the supervision of T.S. and G.D. All authors have read and given approval to the final version of the manuscript.

Funding Sources

This work was supported by the National Science Foundation (Grant CHE-1710339 to T.C.B) and the German Research Foundation (Grant FOR 1530 to C.K., T.S., and G.D.).

Notes

The authors declare no competing financial interest.

ACKNOWLEDGMENT

The authors thank Dr. Nuru Stracey for collecting preliminary MCD spectra of PceA.

ABBREVIATIONS

RDases, reductive dehalogeneases; Cbl^*, norpseudocobalamin; PCE, tetrachloroethylene; TCE, trichloroethylene; DCE, dichloroethylene; SET, single electron transfer; MCD, magnetic circular dichroism; QM/MM, quantum mechanics/molecular mechanics; Cbi, cobinamide; Abs, electronic absorption; CD, circular dichroism; rmsd, root mean squared deviation; TD-DFT, time-dependent density functional theory; EDDM, electron density difference map; $Co(II)Cbi^+$, Co(II)cobinamide; MLCT, metal to ligand charge transfer; MO, molecular orbital; DBE, dibromoethylene; ATRs, adenosyltransferases.

REFERENCES

1. Holliger, C., Wohlfarth, G. & Diekert, G. (1999) Reductive Dechlorination in the Energy Metabolism of Anaerobic Bacteria. *FEMS Microbiol. Rev.* **22**, 383–398.
2. John, M., Rubick, R., Schmitz, R. P. H., Rakoczy, J., Schubert, T. & Diekert, G. (2009) Retentive Memory of Bacteria: Long-Term Regulation of Dehalorespiration in Sulfurospirillum multivorans. *J. Bacteriol.* **191**, 1650–1655.
3. Abrahamsson, K., Ekdahl, A., Collén, J. & Pedersén, M. (1995) Marine Algae-A Source of Trichloroethylene and Perchloroethylene. *Limnol. Oceanogr.* **40**, 1321–1326.
4. Field, J. A. (Springer Berlin Heidelberg, 2016). Natural Production of Organohalide Compounds in the Environment. in *Organohalide-Respiring Bacteria* (eds. Adrian, L. & Löffler, F. E.) 7–29 doi:10.1007/978-3-662-49875-0_2.
5. Neumann, A., Wohlfarth, G. & Diekert, G. (1995) Properties of Tetrachloroethene and Trichloroethene Dehalogenase of

Dehalospirillum multivorans. *Arch Microbiol* **163**, 276–281.
6. Scholz-Muramatsu, H., Neumann, A., Meßmer, M., Moore, E. & Diekert, G. (1995) Isolation and Characterization of *Dehalospirillum multivorans* gen. nov., sp. nov., a Tetrachloroethene-Utilizing, Strictly Anaerobic Bacterium. *Arch Microbiol* **163**, 48–56.
7. Goris, T., Schubert, T., Gadkari, J., Wubet, T., Tarkka, M., Buscot, F., Adrian, L. & Diekert, G. (2014) Insights Into Organohalide Respiration and the Versatile Catabolism of *Sulfurospirillum multivorans* Gained From Comparative Genomics and Physiological Studies. *Environ. Microbiol.* **16**, 3562–3580.
8. Fincker, M. & Spormann, A. M. (2017) Biochemistry of Catabolic Reductive Dehalogenation. *Annu. Rev. Biochem.* **86**, 357–386.
9. Schubert, T., Adrian, L., Sawers, R. G. & Diekert, G. (2018) Organohalide Respiratory Chains: Composition, Topology and Key Enzymes. *FEMS Microbiol. Ecol.* **94**, 10.1093/femsec/fiy035.
10. Krautler, B., Fieber, W., Ostermann, S., Fasching, M. & Ongania, K.-H. (2003) The Cofactor of Tetrachloroethene Reductive Dehalogenase of *Dehalospirillum multivorans* Is Norpseudo-B_{12}, a New Type of a Natural Corrinoid. *Helv. Chim. Acta* **86**, 3698–3716.
11. Bommer, M., Kunze, C., Fesseler, J., Schubert, T., Diekert, G. & Dobbek, H. (2014) Structural Basis for Organohalide Respiration. *Science* **346**, 455–458.
12. Kunze, C., Bommer, M., Hagen, W. R., Uksa, M., Dobbek, H., Schubert, T. & Diekert, G. (2017) Cobamide-Mediated Enzymatic Reductive Dehalogenation via Long-Range Electron Transfer. *Nat. Commun.* **8**, 1–11.
13. Diekert, G., Boland, W., Svatos, A., Ploss, K., Neumann, A., Habel, A., Wolf, J., Schmidtz, R. P. H., Schmitz, R. P. H., Wolf, J., Habel, A., Neumann, A., Ploss, K., Svatos, A., Boland, W. & Diekert, G. (2007) Evidence for a Radical Mechanism of the Dechlorination of Chlorinated Propenes Mediated by the Tetrachloroethene Reductive Dehalogenase of *Sulfurospirillum multivorans*. *Environ. Sci. Technol.* **41**, 7370–7375.
14. Lihl, C., Douglas, L. M., Franke, S., Pérez-De-Mora, A., Meyer, A. H., Daubmeier, M., Edwards, E. A., Nijenhuis, I., Sherwood Lollar, B. & Elsner, M. (2019) Mechanistic Dichotomy in Bacterial Trichloroethene Dechlorination Revealed by Carbon and Chlorine Isotope Effects. *Environ. Sci. Technol.* **53**, 4245–4254.
15. Heckel, B., McNeill, K. & Elsner, M. (2018) Chlorinated Ethene Reactivity with Vitamin B_{12} Is Governed by Cobalamin Chloroethylcarbanions as Crossroads of Competing Pathways. *ACS Catal.* **8**, 3054–3066.
16. Renpenning, J., Keller, S., Cretnik, S., Shouakar-Stash, O., Elsner, M., Schubert, T. & Nijenhuis, I. (2014) Combined C and Cl Isotope Effects Indicate Differences between Corrinoids and Enzyme (*Sulfurospirillum multivorans* PceA) in Reductive Dehalogenation of Tetrachloroethene, But Not Trichloroethene. *Environ. Sci. Technol.* **48**, 11837–11845.
17. Liao, R.-Z., Chen, S.-L. & Siegbahn, P. E. M. (2016) Unraveling the Mechanism and Regioselectivity of the B_{12}-Dependent Reductive Dehalogenase PceA. *Chem. - A Eur. J.* **22**, 12391–12399.
18. Payne, K. A. P., Quezada, C. P., Fisher, K., Dunstan, M. S., Collins, F. A., Sjuts, H., Levy, C., Hay, S., Rigby, S. E. J. & Leys, D. (2015) Reductive Dehalogenase Structure Suggests a Mechanism for B_{12}-Dependent Dehalogenation. *Nature* **517**, 513–516.
19. Liu, C. R., Qian, Y. Y. & Chan, K. S. (2014) Base-Promoted Aryl-Bromine Bond Cleavage with Cobalt(II) Porphyrins via a Halogen Atom Transfer Mechanism. *Dalt. Trans.* **43**, 7771–7779.
20. Gadkari, J., Goris, T., Schiffmann, C. L., Rubick, R., Adrian, L., Schubert, T. & Diekert, G. (2018) Reductive Tetrachloroethene Dehalogenation in the Presence of Oxygen by Sulfurospirillum multivorans: Physiological Studies and Proteome Analysis. *FEMS Microbiol. Ecol.* **94**, https://doi.org/10.1093/femsec/fix176.
21. Zehnder, A. J. B. & Wuhrmann, K. (1976) Titanium(III) Citrate as a Nontoxic Oxidation-Reduction Buffering System for the Culture of Obligate Anaerobes. *Science* **194**, 1165–1166.
22. Seedfeldt, L. & Ensign, S. (1994) A Continuous, Spectrophotometric Activity Assay for Nitrogenase Using the Reductant Titanium(III) Citrate. *Anal. Biochem.* **221**, 379–386.
23. Stich, T. A., Buan, N. R., Escalante-Semerena, J. C. & Brunold, T. C. (2005) Spectroscopic and Computational Studies of the ATP:Corrinoid Adenosyltransferase (CobA) from Salmonella enterica: Insights into the Mechanism of Adenosylcobalamin Biosynthesis. *J. Am. Chem. Soc.* **127**, 8710–8719.
24. Hay, B. P. & Finke, R. G. (1987) Thermolysis of the Co-C Bond in Adenosylcorrins. 3. Quantification of the Axial Base Effect in Adenosylcobalamin by the Synthesis and Thermolysis of Axial Base-Free Adenosylcobinamide. Insights into the Energetics of Enzyme-Assisted Cobalt-Carbon Bond Hom. *J. Am. Chem. Soc.* **109**, 8012–8018.
25. Frisch, M. J., Trucks, G. W., Schlegel, H. B., Scuseria, G. E., Robb, M. A., Cheeseman, J. R., Scalmani, G., Barone, V., Mennucci, B., Petersson, G. A., Nakatsuji, H., Caricato, M., Li, X., Hratchian, H. P., Izmaylov, A. F., Bloino, J., Zheng, G., Sonnenberg, J. L., Hada, M., Ehara, M., Toyota, K., Fukuda, R., Hasegawa, Ishida, M., Nakajima, T., Honda, Y., Kitao, O., Nakai, H., Vreven, T., Montgomery, J., J. A., Peralta, J. E., Ogliaro, F., Bearpark, M., Heyd, J. J., Brothers, E., Kudin, K. N., Staroverov, V. N., Keith, T., Kobayashi, R., Normand, J., Raghavachari, K., Rendell, A., Burant, J. C., Iyengar, S. S., Rega, N., Millam, J. M., Klene, M., Knox, J. E., Cross, J. B., Bakken, V., Adamo, C., Jaramillo, J., Gomperts, R., Stratmann, R. E., Yazyez, O., Austin, A. J., Cammi, R., Ochterski, J. W., Martin, R. L., Morokuma, K., Zakrzewski, V. G., Voth, G. A., Salvador, P., Dannenberg, J. J., Dapprich, S., Daniels, A. D., Farkas, O., Foresman, J. B., Ortiz, J. V., Cioslowksi, J. & Fox, D. J. Gaussian 09, Revision D.01, Gaussian, Inc., Wallingford CT.
26. Dolinsky, T. J., Nielsen, J. E., McCammon, J. A. & Baker, N. A. (2004) PDB2PQR: an Automated Pipeline for the Setup, Execution, and Analysis of Poisson-Boltzmann Electrostatics Calculations. *Nucleic Acids Res.* **32**, W665–W667.
27. Schrodinger, L. The PyMOL Molecular Graphics System, 1.3 ed.
28. Reig, A. J., Conrad, K. S. & Brunold, T. C. (2012) Combined Spectroscopic/Computational Studies of Vitamin B_{12} Precursors: Geometric and Electronic Structures of Cobinamides. *Inorg. Chem.* **51**, 2867–2879.
29. Becke, A. D. (1993) Density-Function Thermochemistry 3. The Role of Exact Exchange. *J. Chem. Phys.* **98**, 5648–5652.
30. Perdew, J. P. (1986) Density-Functional Approximation for the Correlation Energy of the Inhomogeneous Electron Gas. *Phys. Rev. B* **33**, 8822–8824.
31. Schaefer, A., Horn, H. & Achlrichs, R. (1992) Fully Optimized Contracted Gaussian Basis Sets for Atoms Lithiium to Krypton. *J. Chem. Phys* **97**, 2571–2577.
32. Cornell, W. D., Cieplak, P., Bayly, C. I., Gould, I. R., Merz, K. M., Ferguson, D. M., Spellmeyer, D. C., Fox, T., Caldwell, J. W. & Kollman, P. A. (1995) A 2nd Generation Force-Field for the Simulation of Proteins, Nucleic-Acids, and Organic-Molecules. *J. Am. Chem. Soc.* **117**, 5179–5197.
33. Marques, H. M., Ngoma, B., Egan, T. J. & Brown, K. L. (2001) Parameters for the AMBER Force Field for the Molecular Mechanics Modeling of the Cobalt Corrinoids. *J. Mol. Struct.* **561**, 71–91.
34. Neese, F. (2012) The ORCA Program System. *Wiley Interdiscip. Rev. Comput. Mol. Sci. 2* 73–78.
35. Yanai, T., Tew, D. P. & Handy, N. C. (2004) A New Hybrid Exchange-Correlation Functional Using the Coulomb-Attenuating Method (CAM-B3LYP). *Chem. Phys. Lett.* **393**, 51–57.
36. Chai, J. D. & Head-Gordon, M. (2008) Systematic Optimization of Long-Range Corrected Hybrid Density Functionals. *J. Chem. Phys.* **128**, 84–106.
37. Weingend, F. & Ahlrichs, R. (2005) Balanced Basis Sets of Split Valence, Triple Zeta Valence and Quadruple Zeta Valence Quality for H to Rn: Design and Assessment of Accuracy. *Phys. Chem. Chem. Phys.* **7**, 3297–3305.
38. Weingend, F. (2006) Accurate Coulomb-Fitting Basis Sets for H to Rn. *Phys. Chem. Chem. Phys.* **8**, 1057–1065.

39. Schäfer, A., Huber, C. & Ahlrichs, R. (1994) Fully Optimized Contracted Gaussian Basis Sets of Triple Zeta Valence Quality for Atoms Li to Kr. *J. Chem. Phys.* **100**, 5829–5835.
40. Pavlova, A., Parks, J. M. & Gumbart, J. C. (2018) Development of CHARMM-Compatible Force-Field Parameters for Cobalamin and Related Cofactors from Quantum Mechanical Calculations. *J. Chem. Theory Comput.* **14**, 784–798.
41. Kieninger, C., Deery, E., Lawrence, A. D., Podewitz, M., Wurst, K., Nemoto-Smith, E., Widner, F. J., Baker, J. A., Jockusch, S., Kreutz, C. R., Liedl, K. R., Gruber, K., Warren, M. J. & Kräutler, B. (2019) The Hydrogenobyric Acid Structure Reveals the Corrin Ligand as an Entatic State Module Empowering B_{12} Cofactors for Catalysis. *Angew. Chemie* **131**, 10869–10873.
42. Stich, T. A., Buan, N. R. & Brunold, T. C. (2004) Spectroscopic and Computational Studies of Co^{2+}Corrinoids: Spectral and Electronic Properties of the Biologically Relevant Base-On and Base-Off Forms of Co^{2+}Cobalamin. *J. Am. Chem. Soc.* **126**, 9735–9749.
43. Liptak, M. D. & Brunold, T. C. (2006) Spectroscopic and Computational Studies of Co^{1+}Cobalamin : Spectral and Electronic Properties of the "Superreduced" B_{12} Cofactor. *J. Am. Chem. Soc.* **128**, 9144–9156.
44. Ye, L. D., Schilhable, A., Bartram, S., Boland, W. & Diekert, G. (2010) Reductive Dehalogenation of Brominated Ethenes by Sulfurospirillum multivorans and Desulfitobacterium hafniense PCE-S. *Enviromental Microbiol.* **12**, 501–509.
45. Lidwig, M., Matthews, R., Huang, S., Drennan, C. & Drummond, J. (1994) How a Protein Binds B_{12}: A 3.0 Å X-Ray Structure of B_{12}-Binding Domains of Methionine Synthase. *Science* **266**, 1669–1674.
46. Pett, V. B., Liebman, M. N., Murray-Rust, P., Prasad, K. & Glusker, J. P. (1987) Conformational Variability of Corrins: Some Methods of Analysis. *J. Am. Chem. Soc* **109**, 3207–3215.
47. Hannibal, L., Smith, C. A., Smith, J. A., Axhemi, A., Miller, A., Wang, S., Brasch, N. E. & Jacobsen, D. W. (2009) High Resolution Crystal Structure of the Methylcobalamin Analogues Ethylcobalamin and Butylcobalamin by X-ray Synchrotron Diffraction. *Inorg. Chem* **48**, 6615.
48. Hodgkin, D. C., Pickworth, J., Robertson, J. H., Trueblood, K. N. & Prosen, R. J. (1955) Structure of Vitamin B_{12}. *Nature* **176**, 325–328.
49. Stich, T. A., Yamanishi, M., Banerjee, R. & Brunold, T. C. (2005) Spectroscopic Evidence for the Formation of a Four-Coordinate Co^{2+}Cobalamin Species upon Binding to the Human ATP:Cobalamin Adenosyltransferase. *J. Am. Chem. Soc.* **127**, 7660–7661.
50. Fonseca, M. V. & Escalante-Semerena, J. C. (2001) An in Vitro Reducing System for the Enzymic Conversion of Cobalamin to Adenosylcobalamin. *J. Biol. Chem.* **276**, 32101–32108.
51. Lexa, D. & Saveant, J.-M. (1983) The Electrochemistry of Vitamin B_{12}. *Acc. Chem. Res* **16**, 235–243.
52. Stich, T. A., Seravalli, J., Venkateshrao, S., Spiro, T. G., Ragsdale, S. W. & Brunold, T. C. (2006) Spectroscopic Studies of the Corrinoid/Iron-Sulfur Protein from *Moorella thermoacetica*. *J. Am. Chem. Soc.* **128**, 5010–5020.
53. Siritanaratkul, B., Islam, S. T. A., Schubert, T., Kunze, C., Goris, T., Diekert, G. & Armstrong, F. A. (2016) Selective, Light-Driven Enzymatic Dehalogenations of Organic Compounds. *RSC Adv.* **6**, 84882–84886.
54. Liao, R. Z., Chen, S. L. & Siegbahn, P. E. M. (2015) Which Oxidation State Initiates Dehalogenation in the B_{12}-Dependent Enzyme NpRdhA: Co^{II}, Co^{I}, or Co^{0}? *ACS Catal.* **5**, 7350–7358.

For Table of Contents Use Only: